A novel tool for simulating brittle borehole breakouts

(article starts on next page)

Research Paper

A novel tool for simulating brittle borehole breakouts

Eleni Gerolymatou

Chalmers University of Technology, Sweden

ARTICLE INFO	ABSTRACT
	Breakouts are important both as a threat to borehole or tunnel stability and as a tool for primary stress state interpretation. This work suggests a semi-analytical method based on conformal mapping for the prediction of breakouts in brittle rock. After introducing the underlying theory, the developed algorithm is outlined. The single components are described and verified. Finally, the applicability and efficiency of the resulting tools is assessed. The aim is to provide a simple, fast and easy to use tool for the assessment of borehole and tunnel stability and for the estimation of the in situ stress in brittle rock.

1. Introduction

Boreholes are in use in a wide variety of applications, ranging from the more conventional site investigations, to deep boreholes operated under variable pressures for energy production, both in the oil and gas industry and for geothermal energy. It is therefore important to be able to assess their stability with confidence, since failure is linked to significant costs.

Before the drilling, the stress state is the initial one, which can be described by the three principal stresses and their directions. The stress state after the construction of the borehole is characterized by a lower minimum principal stress and a higher maximum principal stress, thus increasing the probability of borehole failure. Failure of the borehole wall can be global or local. Local failure, where the global stability is maintained, forms the so-called borehole breakouts. In the direction parallel to the minimum principal stress, failure due to large pressures or shear stresses is likely, while in the direction parallel to the largest principal stress tensile failure is most likely. As a result, the breakouts may vary strongly in shape, see for example [1]. The shape is often used to assess the primary in situ stress [2].

Failure may be ductile or brittle. In both cases, simulation is difficult, in the first case because of the softening of the material and in the second case because of the loss of continuity. In the ductile regime, failure is characterized by zones of localized deformation that cannot be modeled by simple constitutive models in the sense of Noll [3]. Non-local [4], micropolar [5] or higher gradient [6] models have been used so far to simulate the formation of breakouts in materials exhibiting softening. In the brittle regime no solution is yet available, though simulations using discrete elements have attempted to provide an answer [7]. In this case, the limited number of particles that can be used poses a limit to the applicability, since size dependence has been observed both

in situ and in the lab: large boreholes fail at significantly smaller loads than smaller boreholes [8,9]. This effect can however be captured for ductile failure using the non simple models mentioned above. At the same time, a large number of experiments are available from the literature, showing a strong dependence of the shape of the breakouts on the primary stress state, see for example [1]. Conformal mapping has been used before [10] to evaluate the stress field around underground openings. However, the shape of the opening has always been considered known and constant and the provided solutions are only valid for a specific form of the mapping.

In the present work it is attempted to use conformal mapping to model brittle borehole breakouts. The approach presented accounts for the evolution of the shape of the borehole and is valid for arbitrary shapes and mappings. In the next section the general method and the basics of the conformal mapping theory are outlined. The specifics of the method used and details concerning the algorithms, as well as their validations are presented in Section 3. The results are presented and discussed in Section 4. Finally, conclusions are drawn.

2. Method

Breakouts are local failures observed at the wall of the cavity and can vary strongly in shape and intensity. Spiral failure patterns are linked to isotropic primary stress, dog-ear breakouts to shear failure under anisotropic primary stress and slit shaped breakouts to anisotropic stress state with a high mean pressure. Similar effects have been directly observed in tunnels and shafts. Shear and compaction induced breakouts tend to orient themselves parallel to the minimum principal stress. Tensile breakouts, in the form of cracks, tend to orient themselves normal to minimum principal stress. The breakouts linked to isotropic primary stress state lead to complete borehole failure in an

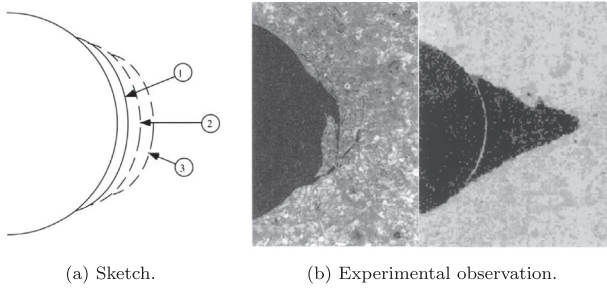(a) Sketch.   (b) Experimental observation.

Fig. 1. Breakout evolution after [11].

elastic-perfectly brittle material and will not be considered here.

It is known, that the width of the breakouts remains constant during the procedure of the breakout formation, as shown by [11], see Fig. 1. The material tested in this case was limestone. This means that the width of the breakout can be determined using the analytical solutions available in elasticity for the stress state around a circular opening under plane strain conditions. Here conformal mapping is used to simulate the progressive formation of breakouts, including their depth and precise shape. The algorithm developed and the basic underlying theory are given in the rest of the present section.

2.1. Algorithm

The algorithm developed is summarized below in pseudo-code. The single elements are presented in detail and validated in the next section.

Data: primary stress, yield condition, discretization

Result: final borehole shape and stress state

begin

    initialization;

    evaluate secondary stress state;

    remove the part that failed;

    measure the surface that was lost S;

    while $S > precision$ **do**

        evaluate the conformal mapping;

        evaluate the new stress state;

        remove the part that failed;

        measure the surface that was lost S;

    end

end

output the final curve and stress distribution;

2.2. Conformal mapping

Here the application of conformal mapping to elastic solids is summarized. A more extended introduction to the topic may be found in [12,13]. It is well known from the theory of elasticity that the stresses in a planar elastic medium can be written as

$$\sigma_{xx} = \frac{\partial^2 U}{\partial y^2}, \quad \sigma_{yy} = \frac{\partial^2 U}{\partial x^2}, \quad \sigma_{xy} = -\frac{\partial^2 U}{\partial x \partial y} \tag{1}$$

where $U(x, y)$ is an appropriate solution of the biharmonic equation. The solution may be expressed in terms of analytic functions as

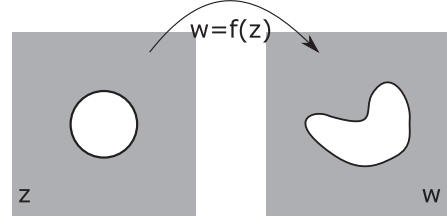$$U(z) = \Re[\bar{z}\phi(z) + \chi(z)] \tag{2}$$

For the stresses it results that

Fig. 2. Mapping from the reference to the target domain.

$$\sigma_{xx} + \sigma_{yy} = 4Re[\phi'(z)] \tag{3}$$

$$\sigma_{yy} - \sigma_{xx} + 2i\sigma_{xy} = 2[\bar{z}\phi''(z) + \chi'(z)] \tag{4}$$

where the functions $\phi(z)$ and $\chi(z)$ must be such as to satisfy the boundary condition

$$i \int_S \left(f_x + if_y\right) ds = \phi(z) + z\overline{\phi'(z)} + \overline{\chi(z)} \tag{5}$$

where f_x and f_y are the horizontal and vertical components of the tractions acting on the boundary S.

The solution of the above is difficult, when the boundary is irregularly shaped. An obvious solution is to use a mapping to solve the problem in a reference domain with more regular geometry. Consider z to be the reference domain and w to be the domain in which the solution is sought, as shown for example in Fig. 2. It is assumed that the following conformal map is known

$$w = f(z) \tag{6}$$

Denote by $\phi_1(z), \chi_1(z)$ the functions written earlier as $\phi(z), \chi(z)$ and introduce the new notation

$$\phi(w) = \phi_1(z) = \phi_1(\omega(w)), \quad \chi(w) = \chi_1(z) = \chi_1(\omega(w)) \tag{7}$$

Expressing the solution in the w-domain in terms of the solution in the z-domain yields

$$\sigma_{xx} + \sigma_{yy} = 4Re\left[\phi'(w)\right] = 4\Re\left[\phi_1'(z)\frac{dz}{dw}\right] = 4\Re\left[\frac{\phi_1'(z)}{f'(z)}\right] \tag{8}$$

$$\sigma_{yy} - \sigma_{xx} + 2i\sigma_{xy} = 2[\bar{w}\phi''(w) + \chi'(w)] \Rightarrow \tag{9}$$

$$\sigma_{yy} - \sigma_{xx} + 2i\sigma_{xy} = 2\left[\bar{w}\frac{\phi_1''(z)f'(z) - \phi_1'(z)f''(z)}{f'(z)^3} + \frac{\chi_1'(z)}{f'(z)}\right] \tag{10}$$

The boundary condition that needs to be satisfied then reads

$$\phi_1(z) + \frac{f(z)}{\overline{f'(z)}}\overline{\phi_1'(z)} + \overline{\chi_1(z)} = i \int (f_x + if_y) ds \tag{11}$$

In the present work this method will be used to map the exterior of a borehole with breakouts to the exterior of the unit circle and evaluate the stress state in the target domain.

3. Theory and calculation

For the present analysis it is assumed that plane strain is a good approximation of the in situ conditions, that the material response is elastic-perfectly brittle and that the material surrounding the borehole is isotropic, as far as its elastic response is concerned. Anisotropy can be incorporated in solutions using the method of conformal mapping, but such methods were not used here.

3.1. Evaluation of the conformal map

The goal is to find a mapping of the form

$$w = \sum_{n=0}^{k} q_n z^{1-n} \tag{12}$$

that will map the unit circle $|z| = 1$ on the desired boundary in the w-space. Let

$$z = r \cdot e^{i\theta}, \quad w = \rho \cdot e^{i\omega} \tag{13}$$

i.e. the arguments of z and w do not necessarily coincide.

A variant of the method of simultaneous equations is used here, introduced by Kantorovich [14]. The variation is introduced, because the goal is to map the exterior of the actual geometry to the exterior of the unit circle, rather than considering the interiors. The actual boundary can theoretically be expressed as a real function of the angle θ and the same holds for its square. Thus, the curve of the boundary can be expressed as

$$w \cdot \bar{w} - R(\omega)^2 = w \cdot \bar{w} - F(\theta) = 0 \tag{14}$$

The function F can be expressed on approximation as a truncated Fourier series of the form

$$F(\theta) = \sum_{n=-k}^{k} c_n e^{in\theta} \tag{15}$$

either using a Fast Fourier Transform or a least squares approximation. An approximate mapping of the form

$$w = \sum_{n=0}^{k} q_n z^{1-n} \tag{16}$$

is sought, which, for $|z| = 1$ can be expressed as

$$w = \sum_{n=0}^{k} q_n e^{i(1-n)\theta} \tag{17}$$

Introducing the above in Eq. (14), one gets after some manipulation,

$$\sum_{n=0}^{k} q_n e^{i(1-n)\theta} \sum_{m=0}^{k} \bar{q}_m e^{i(m-1)\theta} = \sum_{n=-k}^{k} c_n e^{in\theta} \Rightarrow \tag{18}$$

$$\sum_{n=0}^{k} \sum_{m=n}^{k} q_{m-n} \bar{q}_m e^{in\theta} + \sum_{n=0}^{k} \sum_{m=n}^{k} q_m \bar{q}_{m-n} e^{-in\theta} = \sum_{n=0}^{k} c_n e^{in\theta} + \bar{c}_n e^{-in\theta} \tag{19}$$

Equating the terms with the same exponents, yields the following system of $k + 1$ equations, with $n \in \{0, 1, ..., k\}$

$$\sum_{m=n}^{k} q_{m-n} \bar{q}_m = c_n \tag{20}$$

Assuming the complex coefficients to be of the form

$$q_m = p_m + i s_m \tag{21}$$

where p_m and s_m are real numbers, the above product may be written as

$$\sum_{m=n}^{k} (p_{m-n} p_m + s_{m-n} s_m) = \Re(c_n) \tag{22}$$

$$\sum_{m=n}^{k} (s_{m-n} p_m - s_m p_{m-n}) = \Im(c_n) \tag{23}$$

The last equation is indeterminate for $n = 0$, meaning that the number of equations is by one smaller than the number of unknowns. A common assumption, and the one used here, is to set equal to zero the imaginary part of the first term of the series. A nonzero imaginary part would imply a rotation. In such a case, an alternative should be selected, such as setting equal to zero the imaginary part of the last, rather than the first, term of the series. This is not necessary in the present case, since it is known that the breakouts are aligned to the principal stresses as a rule. The above system can be solved using for example the Newton-Raphson method, which was used here.

This method can be applied when the function $F(\theta)$ is known, which is generally not the case. To circumvent the problem, a procedure similar to the one suggested by Fornberg [15] is used here. The k-roots of unity in the z-space are used for the series expansion. For the first iteration, it is assumed that the arguments correspond with the ones of the corresponding points in the w-space. Then, the method suggested above is used and an approximate mapping is evaluated. The arguments of the points in the w-space are assessed again and the values of the function $F(\theta)$ are evaluated again. The procedure is repeated, until a satisfactory fit is achieved. Due to the fact that the difference in the arguments in the z and w space can be large, a damping factor ζ is used for the Newton-Raphson method.

It is known that the method of successive approximations tends to converge only if the shape to be mapped is relative close to a circle [13]. In addition, it tends to be rather slow, as far as convergence is concerned. Therefore, the method introduced by Fornberg [15] was tested as an alternative. This was found to be significantly faster than the method used here but managed to converge for a much smaller variety of shapes.

3.2. Verification of the mapping

To assess the effectiveness of the code, three different shapes where mapped at different discretizations. The aim is to illustrate the suitability of the code to map different shapes. To this end shapes were used that are common in tunneling or for borehole breakouts. The first is a horse-shoe shaped tunnel, while the other two represent boreholes with dog-ear shaped and slit-shaped breakouts respectively. The parameters α and β are used to describe the shape and their meaning for each shape is illustrated in Fig. 3. Circular segments for which the radius is not given have a radius equal to one. The precision for the series coefficients was set to 10^{-8}, while the error was defined as the mean deviation of the resulting curve from the original one. Some results are presented in Table 1, where k stands for the number of terms in the series approximation, n for the number of points on the curve and ζ for the
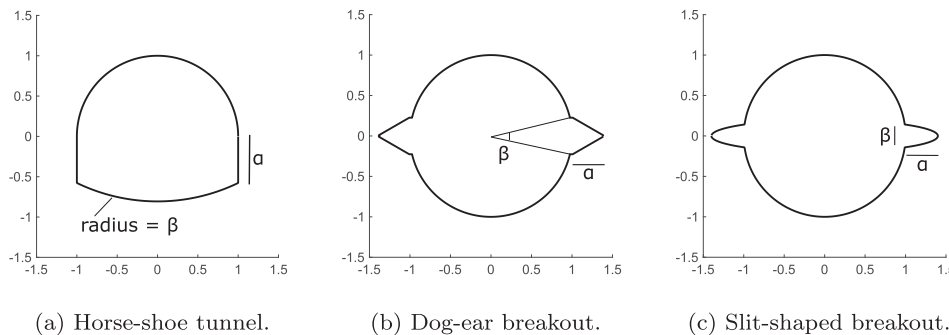

(a) Horse-shoe tunnel. (b) Dog-ear breakout. (c) Slit-shaped breakout.

Fig. 3. Geometries selected for fitting.

Table 1
Conformal map evaluation for different shapes.

Geometry	α	β	n	k	ζ	Iter.	Error	Time [sec]
1	0.5	2.3	512	10	0.5	10	1.6e−04	0.58
1	0.5	2.3	1024	10	0.5	9	1.14e−04	1.42
1	0.5	2.3	512	100	0.5	12	2.00e−06	0.87
2	0.4	$\pi/6$	1024	10	0.5	2	1.3e−03	0.57
2	0.4	$\pi/6$	1024	100	0.5	max	1.3e−03	24.19
2	0.4	$\pi/6$	1024	100	0.1	53	4.2629e−05	1.77
3	0.4	0.2	1024	100	0.02	281	8.8359e−05	7.79
3	0.4	0.2	1024	100	0.01	516	8.8260e−05	13.30
3	0.4	0.2	1024	200	0.01	275	4.1508e−05	17.81
3	0.6	0.2	1024	200	0.01	324	6.4821e−05	20.74
3	0.8	0.2	1024	200	0.01	384	7.2559e−05	24.47
3	1.0	0.4	1024	200	0.01	468	8.8358e−05	29.06

relaxation factor used. The last shape was found to be the most challenging to fit. The time was measured on a personal computer and is indicative. Some examples are shown in Fig. 4. As seen in Fig. 4a the quality of the fit improves with increasing number of series terms, especially where the shape has angles. As would be expected, the time necessary for the fit increases with increasing number of terms and increasing number of input points for the curve. A larger value of ζ leads to faster convergence, but decreases the likelihood for the solution to be reached. This is especially the case for shapes such as the second and third step considered here. In fact, the second shape fails to converge with a value of ζ equal to 0.5, but converges when ζ is set to 0.1, at an additional cost in terms of time. As may be seen in Fig. 4b, the failure to converge is a result of argument miscalculation. Examples for theborehole with slit-shaped breakouts are shown in Fig. 4c for increasing depths of the breakout. The fit remains satisfactory, but requires a small value of ζ and therefore also a larger number of iterations and longer times to converge. It would be possible to reduce the time required to calculate the mappings for such shapes, which deviate strongly from the circle, by varying ζ, selecting a small value for the first iterations and increasing values for the subsequent ones. This was not attempted here.

On the whole, the algorithm for the evaluation of the conformal maps performs satisfactorily, even for shapes that deviate significantly from the circle, as shown in Fig. 4c, where the maximum depth of the slit-shaped breakout is equal to the radius of the borehole.

3.3. Evaluation of the stress state

Here the solution is mapped from the exterior of a borehole with breakouts to the exterior of the circle. z is the domain expressing the exterior of the circle and w is the domain in which the solution is sought. It is known that w can be expressed as a series expansion with respect to z with the form

$$w = \sum_{n=0}^{\infty} q_n z^{1-n} \tag{24}$$

In the above equation, it is possible to retain only certain exponents, exploiting symmetry, thus reducing the size of the problem. For the sake of generality, all terms are retained here.

In the z domain the solution is of the form

$$\phi_1(z) = Az + \sum_{n=1}^{\infty} A_n z^{1-n} \tag{25}$$

and

$$\chi_1(z) = Bz + \sum_{n=1}^{\infty} B_n z^{1-n} \tag{26}$$

The first derivatives of the above functions read

$$\phi_1'(z) = A + \sum_{n=1}^{\infty} \left(1 - n\right) A_n z^{-n} = A + \sum_{n=1}^{\infty} a_n z^{-n} \tag{27}$$

and

$$\chi_1'(z) = B + \sum_{n=1}^{\infty} \left(1 - n\right) B_n z^{-n} = B + \sum_{n=1}^{\infty} b_n z^{-n} \tag{28}$$

The boundary solution at infinity implies that

$$A = \frac{\sigma_v + \sigma_h}{4} R \tag{29}$$

$$B = \frac{\sigma_v - \sigma_h}{2} R \tag{30}$$

while it will also hold that

$$A_1 = B_1 = 0 \tag{31}$$

to restrict rigid displacements and rotations.

The boundary condition at the circle boundary can be derived from the expression

$$\phi_1(z) + \frac{f(z)}{\overline{f'(z)}} \overline{\phi_1'(z)} + \overline{\chi_1(z)} = i \int (f_x + if_y) ds \tag{32}$$

In the case of an internal cavity under uniform pressure this yields

$$\phi_1(z) + \frac{f(z)}{\overline{f'(z)}} \overline{\phi_1'(z)} + \overline{\chi_1(z)} = p_0 w = p_0 f(z) \Rightarrow \tag{33}$$

$$\overline{f'(z)} \phi_1(z) + f(z) \overline{\phi_1'(z)} + \overline{f'(z)} \overline{\chi_1(z)} - p_0 f(z) \overline{f'(z)} = 0 \tag{34}$$

In Eq. (34), which expresses the boundary condition, each of the terms will be expressed as a power series in what follows. Use will be made of the fact that on the boundary

$$z = e^{i\theta}$$

since we are referring to the unit circle. The series are truncated, as necessary for numerical evaluation. The coefficients of the mapping are
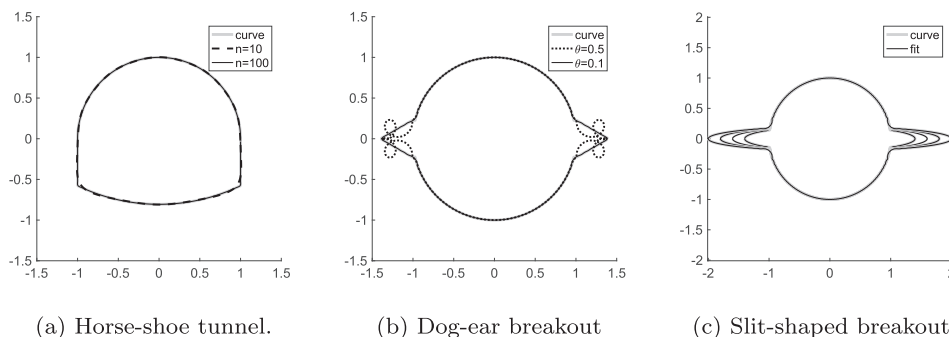

(a) Horse-shoe tunnel.   (b) Dog-ear breakout   (c) Slit-shaped breakout.

Fig. 4. Shape fitting.

known, as are the first coefficients of the functions ϕ_1 and ψ_1.

$$\overline{f'(z)}\phi_1(z) + f(z)\overline{\phi_1'(z)} + \overline{f'(z)\chi_1(z)} - p_0 f(z)\overline{f'(z)} = 0$$

$$\sum_{n=2}^{k}\sum_{m=0}^{k}\left(1-m\right)A_n\bar{q}_m e^{i(1-n+m)\theta} + \sum_{m=0}^{k}\left(1-m\right)A_0\bar{q}_m e^{i(1+m)\theta}$$

$$+ \sum_{n=2}^{k}\sum_{m=0}^{k}\left(1-n\right)\overline{A}_n q_m e^{i(1-m+n)\theta} + \sum_{m=0}^{k} A_0 q_m e^{i(1-m)\theta}$$

$$+ \sum_{n=2}^{k}\sum_{m=0}^{k}\left(1-m\right)\overline{B}_n\bar{q}_m e^{i(m+n-1)\theta} + \sum_{m=0}^{k}\left(1-m\right)B_0\bar{q}_m e^{i(-1+m)\theta}$$

$$= p_0 \sum_{n=0}^{k}\sum_{m=0}^{k}\left(1-m\right)q_n\bar{q}_m e^{i(1-n+m)\theta}$$

(35)

The above can be solved numerically by equating the exponents of equal order. It results in a linear system of $3k - 1$ equations, or, separating the real from the imaginary parts, $6k - 2$ equations. The unknowns are $2(k - 1)$ complex coefficients or, equivalently, $4(k - 1)$ real ones. It would seem that the system is over-constrained, so that the solution to the corresponding least squares problem is evaluated and provides the coefficients of the functions ϕ_1 and χ_1. Alternatively, it would have been possible to evaluate the series to more than $k + 1$ terms. It is selected here to use the same order of approximation for the mapping and for the functions ϕ_1 and χ_1.

Another possible option would be to assume a discretization of the boundary and to demand Eq. (34) to hold on any point of that discretization. The linear system to be solved will then be over-constrained and the solution returned will be the answer to the corresponding least squares problem. This approach was found to lead to spurious oscillations, due to the fact that terms with higher exponents were favored, depending on the degree to which the system was over-constrained. This led to unrealistic stress oscillations in the vicinity of the boundary.

The semi-analytical approach described above was found to perform better and was retained.

3.4. Verification of the stress state evaluation

To test the implementation, the solution for a crack with half width 1 was compared against the corresponding analytical solution after Kachanov [16]. The external boundary is unloaded and the interior of the crack is subjected to a uniform pressure of measure 1. The conformal map is known and reads

$$w = \frac{1}{2}\left(z + \frac{1}{z}\right)$$

(36)

The result in comparison with the analytical solution for a crack with half-length equal to 1 after [16] is given in Fig. 5. The colormap represents the analytical result, while the isolines marked in white have been evaluated using the algorithm discussed above. As may be observed, the agreement is excellent.

Since the above analytical solution only validates the part linked to the internal pressure, the Kirsch solution for circular openings under

biaxial stress and an analytical solution for an elliptical opening under uniaxial far stress field from [12] is used to validate the evaluation of the stress distribution resulting from the primary stresses.

For the Kirsch solution a horizontal stress of 1 MPa and a vertical stress of 3 MPa are assumed. A series approximation with 20 terms was used. The results are shown in Fig. 6. As may be seen, the absolute error is very small and concentrated around the opening in the form of oscillations.

The solution tested next was that of an ellipse with the expression

$$w = R\left(z + \frac{m}{z}\right)$$

(37)

with $m = 0.5$. The domain is subjected to far-field horizontal stress with a magnitude of 1 MPa. 50 terms were used for the approximation. The mapping was evaluated using the algorithm of the previous section and the result was used for the evaluation of the stress field. The computed solution was compared to the analytical one provided by [12] and the absolute error is plotted in Fig. 7. As may be observed, the absolute error, which is again concentrated in the vicinity of the opening and shows oscillations, remains at all times smaller than 10^{-7}. The same problem was also tackled using an approximation with 20 terms. In this case the maximum absolute error was of the order of 10^{-2}.

In Table 2 the maximum error for different shapes of ellipses and for different numbers of terms used for the mapping is shown. Three different times were measured. Time 1 stands for the whole procedure, including the evaluation of the mapping numerically, as well as the evaluation of the analytical solution for comparison. Time 2 stands for the evaluation of the coefficients of the functions ϕ and χ. Finally, time 3 stands for the evaluation of the stress state, consisting of the summation of the power series required to evaluate the derivatives of the functions ϕ and χ. The first observation to be made is that the maximum error decreases with increasing number of terms as one would expect. It stops decreasing after a certain number of terms, that depends on the shape.

The times were measured at single execution on a personal computer and should thus be considered indicative. Even so it is clear that the time of execution increases with increasing number of terms and with finer discretizations. Another observation that can be made is that the time required for the evaluation of the series coefficients of the stress functions is only a small fraction of the whole. The largest part of the required time is used for series summation.

On the whole, it may be concluded that the method introduced here provides a good approximation of the stress state around openings of an arbitrary shape.

3.5. Oscillation propagation and smoothing

In this section certain points regarding aspects of the implementation other than the conformal mapping are discussed. A significant point concerns spurious oscillations of the solution in the vicinity of the opening.

As shown in Fig. 8a, small oscillations that are not visible in the first iteration propagate and increase in amplitude. This is a result of the
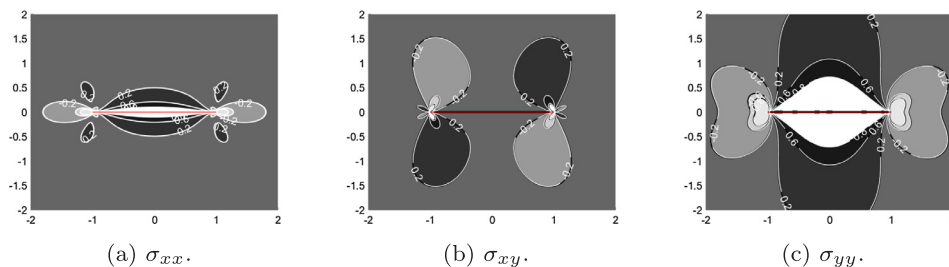

(a) σ_{xx}. (b) σ_{xy}. (c) σ_{yy}.

Fig. 5. Quasi-analytical approximation results for 25 terms.

(a) σ_{xx}.   (b) σ_{xy}.   (c) σ_{yy}.
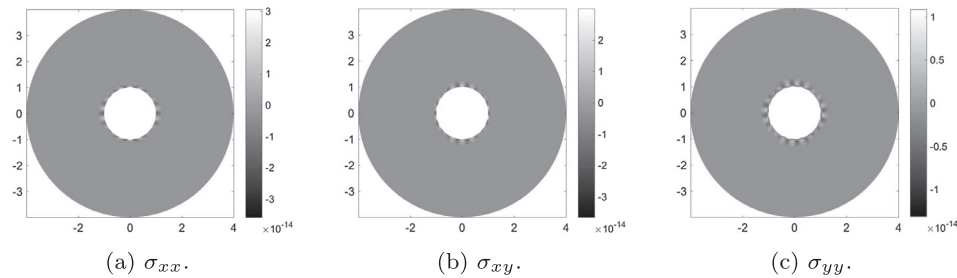
Fig. 6. Absolute error of the computed solution with respect to the Kirsch solution.

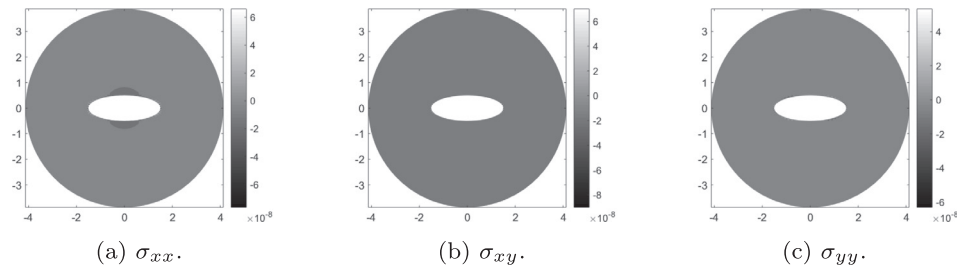(a) σ_{xx}.   (b) σ_{xy}.   (c) σ_{yy}.

Fig. 7. Absolute error of the computed solution with respect to the solution after [12].

Table 2
Stress state accuracy for different ellipses and different numbers of terms.

m	n	k	Max. error	Time 1 [sec]	Time 2 [sec]	Time 3 [sec]
0.2	1024	25	$3.3674e-06$	1.974315	0.022092	1.956998
0.2	1024	50	$3.3536e-06$	3.324643	0.012865	3.302847
0.2	1024	100	$3.3536e-06$	6.444014	0.026391	6.429781
0.4	1024	25	$1.7587e-04$	1.744714	0.008909	1.729890
0.4	1024	50	$6.5545e-06$	3.300635	0.010736	3.286997
0.4	1024	100	$6.5587e-06$	6.506391	0.022210	6.492972
0.6	1024	25	$6.9891e-02$	1.717243	0.010161	1.717243
0.6	1024	50	$2.8072e-05$	3.278999	0.010476	3.264389
0.6	1024	100	$9.0391e-09$	6.677930	0.023379	6.663668
0.8	2048	25	$2.3687e+00$	3.544546	0.009983	3.519414
0.8	2048	50	$9.4072e-01$	6.712898	0.012182	6.686189
0.8	2048	100	$5.1216e-03$	13.97138	0.026864	13.94268
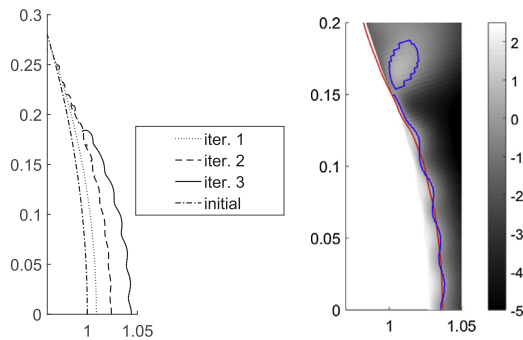
(a) Boundary after successive iterations.   (b) Boundary smoothing.

Fig. 8. Numerical oscillations.

evolution of the boundary shape. Small oscillations present in one iteration mean that the boundary of the next iteration exhibits grooves and peaks, which result in stress concentrations that are not present in reality. Such oscillations become more pronounced as the number of terms used for the series expansion expressing the stress functions increases. As increasing the number of terms of the series expansions however is not practicable beyond a certain point, it was selected to use smoothing in the form of a moving average. An example is shown in

Fig. 8b, where the original curve is shown in blue and the smoothed curve is shown in red. It can also be seen that the blue, original, curve shows stepwise variations in its direction. These are a result of the discretization.

Another feature that can be observed is the formation of areas where the criterion for failure is satisfied, but that are located at the interior of the material. It was selected here to ignore such closed curves. They can however just as easily be included.

4. Results and discussion

The outline of the problem considered is presented in Fig. 9. The geometry is shown in Fig. 9a. The initial borehole radius is set equal to one. This is equivalent to normalizing all length units with the borehole radius. The maximum principal stress, σ_H, is assumed to act in the vertical direction, while the minimum principal stress, σ_h, is assumed to act in the horizontal one. It should be remarked here that rotating the stress state would simply rotate the results by the same angle and in the same direction. Thus, the orientation of the breakouts is the same as one of the principal directions of the in situ stress, in accordance to what has been observed in the field and in the laboratory.

The assumed failure criterion is shown in Fig. 9b. A multi-surface failure criterion was used to render it easy to distinguish between the different modes of failure. A tension cut-off criterion was assumed for tensile failure, a Mohr-Coulomb for shear failure and a circular segment for compaction failure. In all cases arbitrary values were selected for the
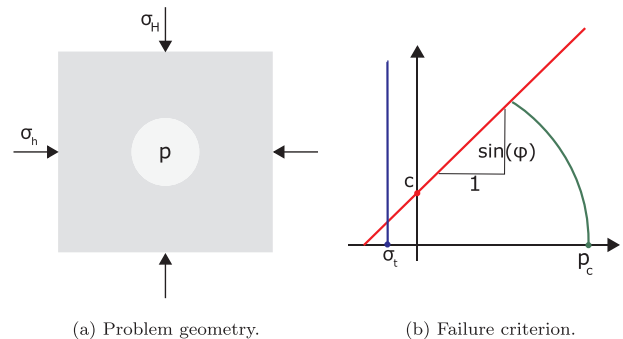

(a) Problem geometry.   (b) Failure criterion.

Fig. 9. Problem outline.

Table 3
Strength parameters.

σ_t [MPa]	c [MPa]	ϕ [°]	p_c [MPa]
6.0	15.0	55	200

strength. The values selected for the tensile and shear strength were chosen close to those measured for different types of granite by [17]. The values used are given in Table 3. Each mode of failure is discussed separately in what follows.

4.1. Shear failure

In Fig. 10 two examples of results are given. The minimum principal stress is set to 20 MPa and maintained constant, while the maximum principal stress ranges from 40 to 50 MPa. The change in both width and depth of the breakouts is easy to note. The different lines in each figure correspond to successive iterations of the code. In Fig. 10a they are not visible due to very fine spacing.

A common reason for simulating borehole breakouts is the assessment of the in situ stress state. As a rule, based on analytical solutions, only the width can be used, resulting in a linear relationship between the principal stresses, rather than in a value for each of the stresses. Based on the Kirsch solution, the circumferential stress at the wall of the borehole is given by

$$\sigma_{\theta\theta} = (\sigma_H + \sigma_h) + 2(\sigma_H - \sigma_h)\cos(2\theta) \tag{38}$$

Failure takes place when the uniaxial strength is exceeded. Given that, based on observations, the width of the breakout remains constant while its depth increases, a number of different stress states will result in breakouts with the same width but with different depths. Solving the above for the maximum principal stress yields

$$\sigma_H = \frac{\sigma_{\theta\theta} - (1 - 2\cos(2\theta))\sigma_h}{1 + 2\cos(2\theta)} \tag{39}$$

Substituting the circumferential stress with the uniaxial strength and the angle θ with a selected value yields the locus of stress states resulting in the same width of shear induced breakout. A value of 40° was arbitrarily chosen here and four different stress states were evaluated. They are given in Table 4. The result is shown in Fig. 11. In Fig. 11a the final shapes of the borehole for four different stress states. The numbers in the legend correspond to the enumerated stress states in Table 4. The initial shape is also provided as reference. As may be seen, the width is the same in all cases, but the depth differs. In Fig. 11b the maximum principal stress and the breakout depth are plotted as functions of the minimum principal stress. The corresponding vertical axes are located at the left and the right of the figure, respectively. It is clear that the variation of the breakout depth is nonlinear but has a one to one correspondence to the maximum principal stress.

On the whole the results for shear failure are satisfactory and encourage the possibility of using a formulation such as the one suggested here for the assessment of the in situ stress state on the basis of the shape of borehole breakouts.
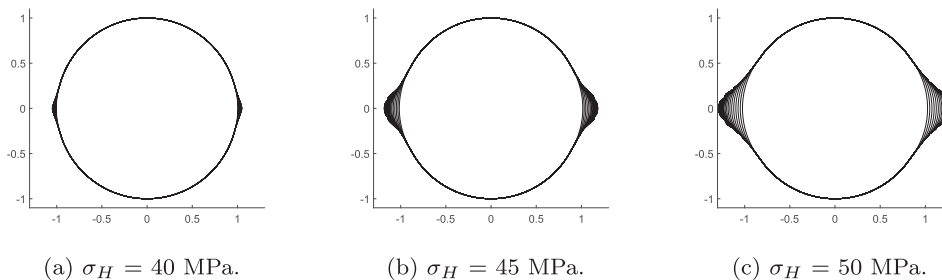
Table 4
Stress states shown in Fig. 11.

	1	2	3	4
σ_h [MPa]	30	35	40	45
σ_H [MPa]	56.088	53.665	51.243	48.821

(a) Breakout shape.　　　(b) Stress states.
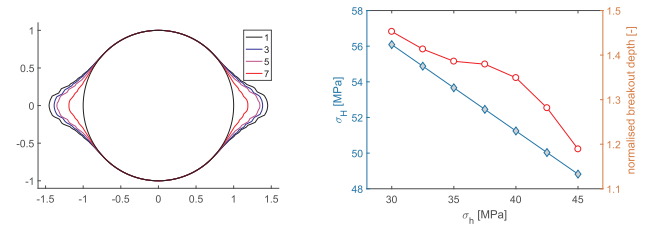
Fig. 11. Effect of the stress state on the breakout depth.
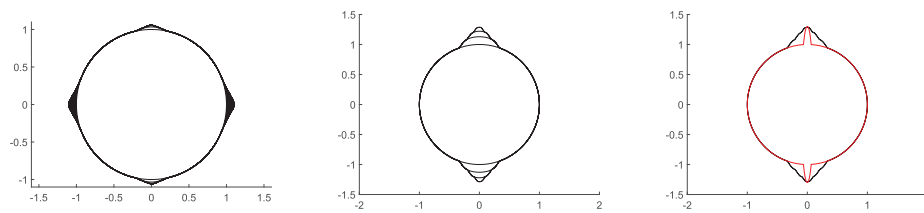
4.2. Tensile failure

Two different primary stress states were considered to test the simulation of tension induced failure. In the absence of internal pressure, tensile stresses appear only if the stress ratio is larger than 3 or smaller than 1/3. The stress states were selected accordingly to ensure that a tensile breakout occurs. For the first of the two, shown in Fig. 12a, it can be observed that both shear induced and tension induced failure take place. Simultaneous occurrence and propagation of breakouts at different locations of the borehole wall pose no difficulties for the implementation.

To investigate more easily the tensile failure mode only, the tension cut off criterion was the only one considered for the next simulation. To test the robustness of the implementations a somewhat extreme stress state was selected with a ratio of maximum to minimum principal stress equal to ten. The result is shown in Fig. 12b. While the simulation converges, the breakout shape differs from the slit shaped breakout known from observations.

The borehole with a narrow breakout shown in Fig. 12c in red and much closer to the typical shape known from observations, was tested under the same stress state. The width was selected small, at 0.1, and the depth was selected equal to the final depth of the breakout shown in Fig. 12b. No failure was found to take place for this shape. This indicates that the code either estimates correctly or overestimates the depth of the tensile breakout.

The origin of the discrepancy in shape may be a result of the selection of the failure criterion, but most likely stems from the fact that in the present work the stress disturbance due to the creation of the borehole was assumed to take place instantaneously.

For tensile failure, where the width of the breakout is known to be extremely small, an analytical evaluation of the conformal map would be more suitable. This can be easily calculated using fist a projection from the shape of the borehole with a slit-shaped breakout to a slit and subsequently from the slit to the unit circle.

(a) $\sigma_H = 40$ MPa.　　　(b) $\sigma_H = 45$ MPa.　　　(c) $\sigma_H = 50$ MPa.

Fig. 10. Shear induced breakouts, $\sigma_h = 20$ MPa.

(a) $\sigma_H = 40$ MPa, $\sigma_h = 10$ MPa. (b) $\sigma_H = 20$ MPa, $\sigma_h = 2$ MPa.   (c) Alternative geometry.

Fig. 12. Tension induced breakouts.
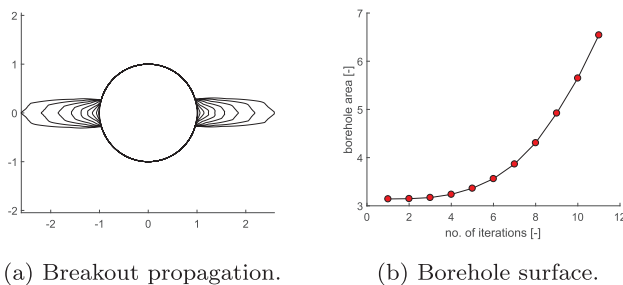
(a) Breakout propagation.   (b) Borehole surface.

Fig. 13. Compaction induced breakouts.

4.3. Compactive failure

Failure due to compaction was investigated next, activating only the relevant yield surface. It was found that the width of the breakout remains constant in this case as well, while the depth increases. In contrast to the results of the previous subsections, the area of material failing at each iteration was found to increase and the propagation of the breakout showed no signs of coming to a stop. An example is shown in Fig. 13, where the minimum principal stress was equal to 90 MPa, while the maximum principal stress was equal to 125 MPa.

In Fig. 13a the evaluated shape of the borehole after successive iterations is shown. While the shape is consistent with the one known from observation, it is clear that the propagation shows to signs of halting. In Fig. 13b the surface of the borehole cross-section (normalized by the square of the borehole radius) is shown as a function of the iterations. The rate of change of the surface seems to be increasing, so that it is obvious that no equilibrium will be reached.

This result may be due to the fact that the material in the present work was considered elastic-perfectly brittle, excluding the possibility of plastic hardening. Another reason for the results observed may be the fact that the out of plane stress was not considered in the calculations.

5. Conclusions

In the present work a semi-analytical method based on conformal mapping was developed for the simulation of borehole breakouts in brittle rock. Breakouts in brittle material were up to now difficult to simulate, due to the loss in continuity in the areas where material failure takes place. The suggested methodology provides a viable solution for such materials at a relatively small numerical cost.

As was shown above, different modes of failure can be simulated, even when taking place at the same time. The proposed method can also capture the breakout depth variation for stress states that are characterized by the same breakout width. This suggests that it may in the future provide a valuable tool for the determination of the in situ stress state on the basis of the shape of the observed borehole breakouts, making use of both width and depth, in contrast to current practice.

The breakouts resulting from tensile failure simulated here were found to be inconsistent in shape with in situ observations. The calculated depth however was shown to be, if not accurate, erring on the safe

side. Possible grounds for the discrepancy may be the selection of failure criterion or the instantaneous unloading assumed in the present work. An analytical calculation of the conformal map can provide the slit-shaped breakouts known from observation.

The implementation presented here presents a significant limitation in that it takes into account only the in plane stresses. The out of plane stress is known to affect the shape of borehole breakouts and the fact that it has not been taken into account in the present work may explain the apparently infinite propagation of compaction induced breakouts observed here. The result may however also be due to the fact that no plastic hardening was considered, as the formulation was developed for the elastic- perfectly brittle materials.

A limitation of conformal mapping that is inherent and cannot be easily addressed, is the failure to account for size effects. This could result in an over-prediction of breakout size for very small boreholes, depending on the characteristic length of the material. Such effects are usually not present for boreholes with a diameter of more than 40 mm, see [18,9]. The problem can be resolved using a suitable failure criterion, for example by using gradient elasticity. Anisotropy in the failure criterion can be incorporated with no difficulty. Anisotropy in the elastic response of the material is however much harder to incorporate and requires a different approach. This is not considered a significant limitation, as in the vast majority of cases the anisotropy of the elastic coefficients in situ is not known and cannot thus be taken into account.

On the whole it can be concluded that the methodology presented here provides a promising tool for the simulation of borehole breakouts in brittle materials.

Acknowledgements

References

[1] Haimson B, Lee H. Borehole breakouts and compaction bands in two high-porosity sandstones. Int J Rock Mech Min Sci 2004;41:287–301.
[2] Valley B, Evans K. Stress state at Soultz-sous-forêts to 5 km depth from wellbore failure and hydraulic observations. Thirty-Second Workshop on Geothermal Reservoir Engineering. Stanford, California: Stanford University; 2007. pp. SGP–TR–183.
[3] Noll W. A new mathematical theory of simple materials. Arch Ration Mech Anal 1972;48:1–50.
[4] Crook T, Willson S, Jian G, Owen R. Computational modelling of the localized deformation associated with borehole breakout in quasi-brittle materials. J Petrol Sci Eng 2003;38:177–81.
[5] Papamichos E. Borehole failure analysis in a sandstone under anisotropic stresses. Int J Numer Anal Meth Geomech 2010;34:581–603.
[6] Zervos A, Papanastasiou P, Vardoulakis I. Modelling of localisation and scale effect in thick-walled cylinders with gradient elastoplasticity. Int J Solids Struct 2001;38:5081–95.
[7] Lee H, Moon T, Haimson B. Borehole breakouts induced in arkosic sandstones and a discrete element analysis. Rock Mech Rock Eng 2016;49:1369–88.
[8] Cuss R, Rutter E, Holloway R. Experimental observations of the mechanics of borehole failure in porous sandstone. Int J Rock Mech Min Sci 2003;40:747–61.
[9] Meier T, Rybacki E, Reinicke A, Dresen G. Influence of borehole diameter on the

formation of borehole breakouts in black shale. Int J Rock Mech Min Sci 2013;62:74–85.

[10] Exadaktylos G, Stavropoulou M. A closed-form elastic solution for stresses and displacements around tunnels. Int J Rock Mech Min Sci 2002;39:905–16.

[11] Zoback M, Barton C, Brudy M, Castillo D, Finkbeiner T, Grollimund B, et al. Determination of stress orientation and magnitude in deep wells. Int J Rock Mech Min Sci 2003;40:1049–76.

[12] Muskhelishvili N. Some basic problems of the mathematical theory of elasticity. Springer; 2010.

[13] Schinzinger R, Laura P. Conformal mapping: methods and applications. Elsevier Science Publishers B.V.; 1991.

[14] Kantorovich L. On some methods of constructing a function effecting a conformal transformation. Bull Acad Sci USSR 1933;7:229–35.

[15] Fornberg B. A numerical method for conformal mapping. SIAM J Sci Stat Comput 1980;1:386–400.

[16] Kachanov M. Elastic solids with many cracks and related problems. Adv Appl Mech 1994;30:259–445.

[17] Arzúa J, Alejano L. Dilation in granite during servo-controlled triaxial strength tests. Int J Rock Mech Min Sci 2013;61:43–56.

[18] Dresen G, Stanchits S, Rybacki E. Borehole breakout evolution through acoustic emission location analysis. Int J Rock Mech Min Sci 2003;47:426–35.